Advances in Power Systems Research
https://apsr.cultechpub.com/apsr
Cultech Publishing

Article

Adaptive Vector Control of VSC-HVDC Systems Using Lightweight Fuzzy Q-Learning

Ganesh Moorthy Jagadeesan*, Vani Easwaran

Department of Electrical and Electronics Engineering, KSR College of Engineering, Tiruchengode, India

*Corresponding author: Ganesh Moorthy Jagadeesan, jp.ganesh11@gmail.com

Abstract

This paper presents an adaptive vector control framework for Voltage Source Converter-based High Voltage Direct Current (VSC-HVDC) systems using a novel Lightweight Fuzzy-Enhanced Q-Learning (LFQL) controller. The proposed LFQL architecture integrates a fuzzy inference layer with a reinforcement learning (RL) agent to enable real-time self-tuning of current and voltage references, overcoming the limitations of conventional fixed-gain PI controllers. Designed for bidirectional power transfer and asynchronous grid interconnection, the controller ensures robust regulation of DC-link voltage and accurate tracking of active and reactive power under dynamic grid conditions. Comparative simulation results highlight the advantages of LFQL over traditional PI control: settling time for DC-link voltage is reduced from 0.45 s to 0.21 s, reactive power overshoot drops from 7.8% to 2.3%, and active power steady-state error is limited to below 0.5%. Furthermore, the LFQL control scheme maintains waveform integrity and dynamic stability even during frequency mismatch and power reversal scenarios. Its low computational footprint and superior adaptability make LFQL a practical and scalable solution for intelligent HVDC control in evolving power systems.

Keywords

Adaptive control, Fuzzy logic, Q-Learning, Smart grid, VSC-HVDC

Article History

Received: 17 May 2025
Revised: 10 June 2025
Accepted:19 June 2025
Available Online: 25 June 2025

Copyright

1. Introduction

1.1 Research Background

The global transition toward decentralized, clean energy systems has presented new challenges for traditional Alternating Current (AC) transmission systems. The integration of renewable energy sources (RESs), offshore wind farms, and asynchronous networks requires enhanced controllability and resilience in power transmission architectures [1]. Conventional AC systems struggle under low-inertia conditions, with limited frequency support and reactive power management capabilities [2].

Voltage Source Converter-based High Voltage Direct Current (VSC-HVDC) systems have emerged as a pivotal solution, offering independent control of active and reactive power, low harmonic distortion, compact design, and suitability for weak grid integration [3]. VSC-HVDC is also uniquely equipped with black-start capability, modular scalability, and bidirectional power flow features [4]. These characteristics make it ideal for offshore renewable integration, long-distance power transfer, and multi-terminal DC grid development [5].

Several works affirm that VSC-HVDC systems improve the dynamic stability, inertia response, and operational flexibility of power systems transitioning to low-carbon and high-renewable configurations [6]. The convergence of policy mandates (e.g., UN SDG 7 and SDG 13) with technology maturity further motivates the adoption of VSC-HVDC infrastructure in smart grids [7].

1.2 Literature Review

The most widely adopted control scheme in VSC-HVDC systems is the vector control method, implemented in the dq reference frame and governed by Proportional-Integral (PI) controllers [8]. PI-based control is effective in steady-state operation but falters under fast dynamics like power reversal, fault conditions, or grid disturbances due to its linear design and limited adaptability [9].

To overcome these limitations, researchers have proposed various advanced control techniques. Model Predictive Control (MPC) offers strong predictive accuracy and constraint handling but demands high computational power, limiting its real-time feasibility [10]. Direct Power Control (DPC) achieves fast response but introduces significant switching ripple and harmonic content [11]. Sliding Mode Control (SMC), known for robustness against parameter variations, is hindered by chattering and implementation difficulty [12].

In parallel, AI-based methods have gained traction. Fuzzy Logic Controllers (FLCs) are praised for handling nonlinearities and being computationally light, but their rule base remains fixed and non-adaptive [12]. Artificial Neural Networks (ANNs) provide powerful function approximation and adaptability, but they suffer from black-box behavior, need for training data, and high memory requirements [13].

Reinforcement Learning (RL) [14], particularly Q-Learning [15], has been employed to tune controllers online without explicit system modeling. However, it faces challenges like slow convergence and large action spaces, which constrain deployment in embedded applications. Hybrid models, such as fuzzy-Q-learning systems, have been proposed to merge interpretability with learning capability, but most studies address limited subsystems and avoid full vector control integration [16].

1.3 Research Gaps and Challenges

Despite technological advances, significant gaps remain in the design of adaptive controllers for VSC-HVDC systems. Most AI-based controllers either demand extensive offline training or are too computationally expensive for real-time applications on digital signal processors (DSPs) or Field Programmable Gate Array (FPGAs) [17]. Pure fuzzy logic systems, while light, cannot adapt to changing grid conditions [18], whereas standalone Q-learning agents often exhibit high latency in decision-making, especially during transient events [19].

Another major limitation is the scope of integration many studies focus on partial control layers (e.g., voltage stability, power sharing) instead of full vector control integration under dynamic grid scenarios [20]. Additionally, most hybrid schemes suffer from poor scalability, requiring careful tuning or excessive hyperparameter optimization that reduces generalizability [21]. There is a critical need for an adaptive and intelligent controller that is lightweight, computationally efficient, and easily integrated into the vector control loop. It must remain robust under disturbances such as grid faults, power reversals, and varying RES behavior.

1.4 Motivation

The deployment of intelligent controllers in VSC-HVDC systems remains constrained by the trade-off between adaptability and real-time feasibility. PI and fuzzy-only controllers are lightweight but lack adaptability, while deep learning and full RL systems are too computationally heavy for embedded use [22]. Power system operation increasingly demands controllers that can self-tune during runtime, respond to unforeseen disturbances, and maintain grid stability without manual reconfiguration [23].

This research is driven by the need to bridge this trade-off, targeting a solution that combines learning and interpretability without high computational load. Inspired by human-like decision-making, the proposed controller uses fuzzy logic for real-time action selection and Q-learning for online policy adaptation. This hybrid approach ensures both speed and learning efficiency within practical resource limits [24].

1.5 Uniqueness and Key Contributions

The paper introduces the uniqueness and key contributions of the proposed LFQL controller, designed for adaptive vector control in VSC-HVDC systems. The LFQL approach is distinctive in its integration of a fuzzy inference mechanism with a Q-learning agent, allowing the controller to interpret system behavior and adapt its actions in real-time with minimal computational burden. Unlike traditional PI controllers or standalone AI-based solutions, LFQL combines human-like rule-based decision-making with machine learning adaptability, enabling robust control under grid disturbances, power reversals, and load variations. It is optimized for deployment on embedded platforms, thanks to its small memory footprint and fast execution time. Simulation results validate its performance by showing superior dynamic response, reduced settling time, lower overshoot, and enhanced fault resilience compared to conventional and hybrid controllers. These characteristics position LFQL as a practical, scalable, and intelligent control solution for modern HVDC systems operating under increasingly complex and dynamic grid conditions. However, the approach raises questions about its validation in real-world settings, scalability to larger HVDC networks, and the robustness of its reward design under unanticipated grid events.

1.6 Paper Organization

The rest of the paper is structured as follows: Section 2 describes the VSC-HVDC system modeling and control problem formulation. Section 3 details the LFQL controller design, including fuzzy inference and Q-learning algorithm. Section 4 presents simulation results under different operating scenarios. Section 5 evaluates the computational performance and real-time feasibility of LFQL for embedded implementation. Section 6 concludes the paper and outlines directions for future research, including experimental validation and hardware-in-the-loop testing.

2. Vector Control for HVDC

The emergence of VSC-HVDC systems has fundamentally reshaped modern power transmission by enabling compact, modular, and highly controllable solutions capable of independently regulating both active and reactive power. These systems are particularly well-suited for advanced power infrastructure applications, including large-scale renewable energy integration, offshore wind farm connectivity, and the interconnection of asynchronous AC grids. The dynamic behaviour and operational performance of VSC-HVDC systems are primarily dictated by the employed control strategy. Among the various methods, DPC and Vector Control (VC) are the two most widely adopted approaches. DPC is known for its simple structure and fast transient response, as it directly manipulates converter switching states based on instantaneous power measurements. However, its variable switching frequency, limited harmonic performance, and increased computational complexity make it less desirable for grid-scale implementations where stability and waveform quality are essential.

In contrast, Vector Control also known as field-oriented control has become the preferred methodology in VSC-HVDC applications. VC utilizes Clarke and Park transformations to convert three-phase quantities into a synchronously rotating reference frame (dq-frame), effectively decoupling the control of active and reactive power. This decoupling allows for the independent tuning of control loops using PI controllers, which are straightforward to implement and offer precise tracking performance. VC provides enhanced steady-state accuracy, robustness under grid disturbances, and compatibility with high-performance PWM-based modulation schemes. As a result, Vector Control has become the industry standard for high-fidelity and stable VSC-HVDC operation

2.1 Principle of Vector Control

Vector control, also referred to as field-oriented control, is a widely implemented strategy in Voltage Source Converter (VSC)-based systems due to its ability to independently control active and reactive power. The technique involves converting the three-phase (abc) signals into a synchronously rotating reference frame (dq-frame), where the system variables appear as steady-state Direct Current DC quantities. This transformation simplifies control design and enhances both dynamic response and stability.

As illustrated in Figure 1, the transformation framework is built around aligning the rotating dq reference frame with the grid voltage vector. In this configuration, the d-axis component of current (i_d) governs active power, while the q-axis component (i_q) governs reactive power. This orthogonal separation enables independent tuning of each power component using PI controllers, thus facilitating precise power control even under fluctuating grid conditions.

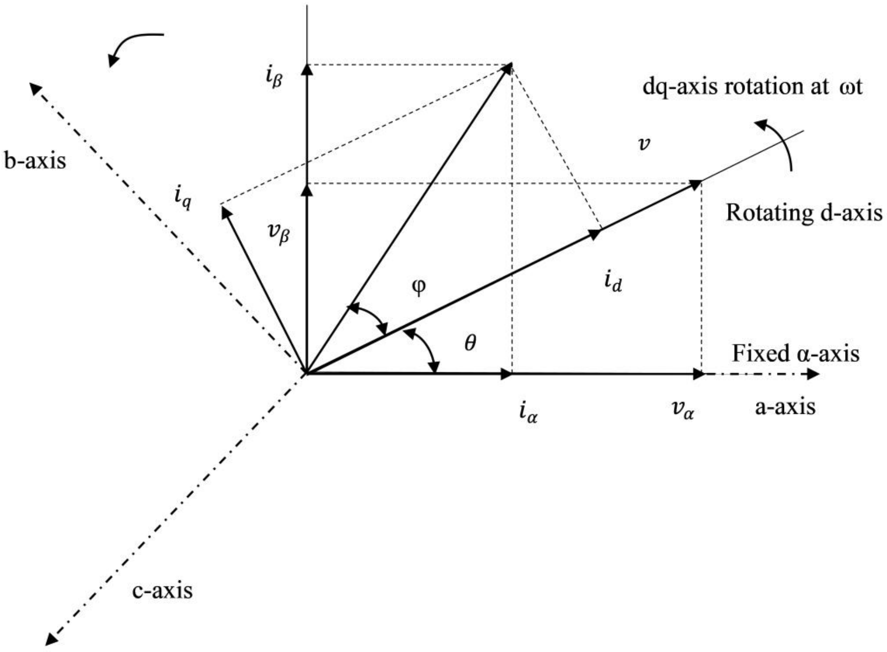

Figure 1. Transformation of axes for vector control in a synchronous rotating reference frame.

The mathematical basis of these transformations is detailed in Table 1. Initially, the Clarke Transformation converts the three-phase (abc) variables into a two-axis stationary αβ-frame. Subsequently, the Park Transformation rotates this αβ frame into the synchronous dq-frame using the instantaneous angle θ = ωt, where ω is the electrical angular frequency. These transformations allow the use of standard linear control techniques in a nonlinear three-phase environment. To apply the control output back to the converter, inverse Park and Clarke transformations are employed to revert the dq control signals to abc voltages for PWM actuation. Overall, vector control enables the VSC to act as a fully controllable voltage source, supporting grid functions such as dynamic voltage regulation, frequency support, and power flow control with high precision and responsiveness.

Table 1. Clarke and park transformations and their corresponding matrix representations.

Transformation	Transforms	Matrix for Transformation
Clark Transformation	from abc to αβ	$\frac{2}{3}\begin{pmatrix}1 & -1/2 & -1/2\\ 0 & \sqrt{3}/2 & -\sqrt{3}/2\end{pmatrix}$
Inverse Clark Transformation	from αβ to abc	$\begin{pmatrix}1 & 0\\ -1/2 & \sqrt{3}/2\\ -1/2 & -\sqrt{3}/2\end{pmatrix}$
Park Transformation	from αβ to dq	$\begin{pmatrix}\cos\theta & \sin\theta\\ -\sin\theta & \cos\theta\end{pmatrix}$
Inverse Park Transformation	from dq to αβ	$\begin{pmatrix}\cos\theta & -\sin\theta\\ \sin\theta & \cos\theta\end{pmatrix}$

2.2 Grid Model

In modern power electronics-based transmission systems such as VSC-HVDC, accurately modeling the electrical behavior of the AC grid is essential for reliable control system design. To achieve this, the AC grid is commonly represented using its Thevenin equivalent, which simplifies the network while retaining the core electrical dynamics critical to power flow and stability analysis.

As depicted in Figure 2, the equivalent per-phase circuit includes an ideal sinusoidal voltage source V_g in series with a resistor R_g and an inductor L_g, representing the grid's internal impedance. These components collectively account for the physical effects of transmission lines, transformers, and nearby generation units. The converter connects to the grid at the Point of Common Coupling (PCC), where the terminal voltage is denoted as V_{PCC} and the current drawn from the grid is represented as i_g.

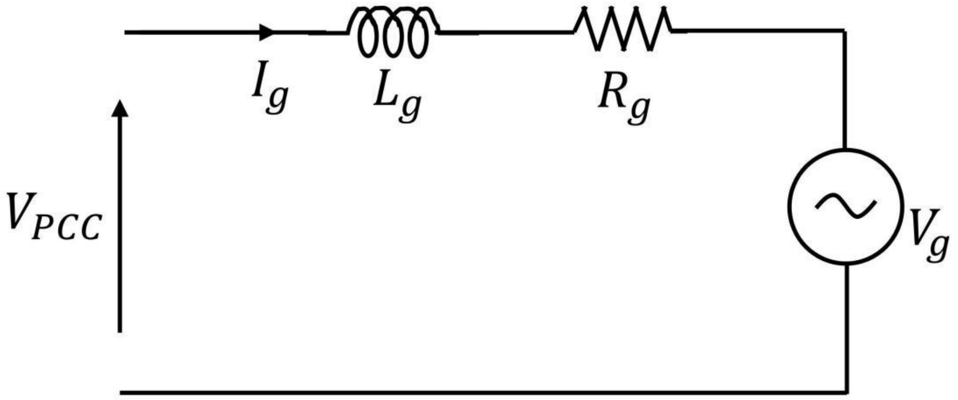

Figure 2. Grid-connected equivalent circuit at PCC.

The voltage equation for this model, derived using Kirchhoff's Voltage Law (KVL), is given as:

$$V_g(t) = R_g \cdot i_g(t) + L_g \cdot \frac{di_g(t)}{dt} + V_{PCC}(t) \quad (1)$$

Where: $V_g(t)$ is the instantaneous grid voltage [V], $i_g(t)$ is the grid current [A], $V_{PCC}(t)$ is the voltage at the PCC [V], R_g is the grid resistance [Ω], L_g is the grid inductance [H].

This model enables accurate transient and frequency-domain analysis of converter-grid interactions, including impedance-based stability assessments, synchronization, and fault response studies. The Thevenin equivalent framework is especially useful in VSC-HVDC simulation environments where the grid must be represented dynamically but without excessive modeling complexity.

2.3 Voltage Source Converter Model

The VSC is the principal component in modular HVDC transmission systems, enabling high-fidelity, bidirectional, and flexible control over power exchange between the AC grid and the DC link. The VSC uses semiconductor-based switching elements to convert AC voltages into controlled DC outputs and vice versa, making it highly suitable for applications involving asynchronous grid interconnections, power flow regulation, and renewable integration.

As illustrated in Figure 3, the modeled converter uses a two-level three-phase VSC topology, which consists of six IGBT switches per converter (two per leg), each with antiparallel diodes to facilitate bidirectional current flow. The AC side of the converter is connected to the grid via coupling components–a series resistor R and inductor L–which emulate line impedance and act as filters to reduce switching noise and protect the converter from grid disturbances.

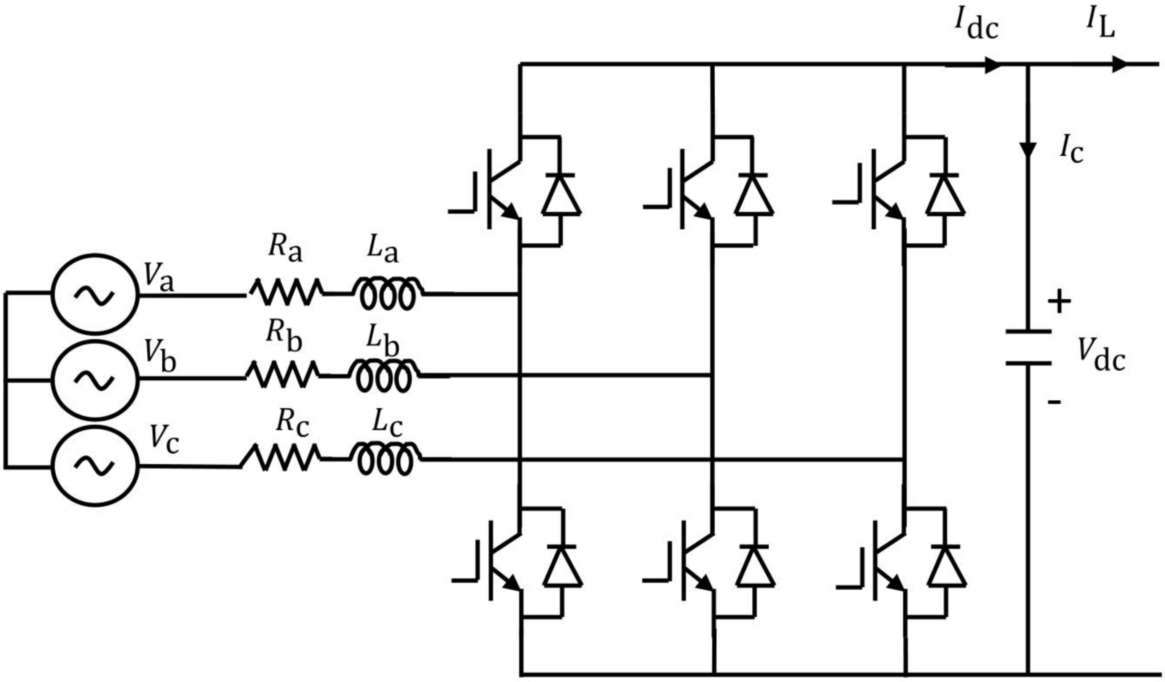

Figure 3. Simplified three-phase VSC topology with grid-side R-L coupling impedance.

The phase-domain voltage dynamics of the converter at the AC interface are described using KVL as:

$$v_g(t) = R \cdot i_g(t) + L \cdot \frac{di_{abc}(t)}{dt} + v_{conv}(t) \quad (2)$$

Where: $v_g(t)$ is the grid-side voltage [V], $v_{conv}(t)$ is the converter terminal voltage [V], $i_g(t)$ is the current flowing into the grid [A].

To decouple active and reactive power control and simplify controller implementation, the three-phase signals are transformed into the synchronously rotating dq-frame using Clarke and Park transformations. Aligning the d-axis with the grid voltage vector, the converter dynamics in this frame are expressed as:

$$L \cdot \frac{di_d}{dt} =- R \cdot i_d - \omega L \cdot i_q - v_{dconv} + v_d \quad (3)$$

$$L \cdot \frac{di_q}{dt} =- R \cdot i_q + \omega L \cdot i_d - v_{qconv} + v_q \quad (4)$$

Here: i_d, i_q: d- and q-axis currents [A], v_d, v_q: d- and q-axis voltages [V], v_{dconv}, v_{qconv}: converter output voltages in dq frame [V], ω: angular grid frequency [rad/s].

The DC side of the VSC is modeled using a capacitor C that maintains a stable DC-link voltage and enables temporary energy storage. The dynamics of this capacitor are governed by:

$$i_{dc} = C \cdot \frac{dV_{dc}}{dt} + I_L \quad (5)$$

Assuming ideal lossless conversion, the instantaneous power balance between AC and DC sides is given by:

$$P_{ac} = V_{dc} \cdot i_{dc} \quad (6)$$

The active and reactive powers at the converter's AC terminal, in dq-frame representation, are computed using:

$$P = \frac{3}{2} v_d \cdot i_d \quad (7)$$

$$Q =- \frac{3}{2} v_d \cdot i_q \quad (8)$$

The reference frame transformation angle θ is determined using the Clarke-transformed voltages v_α and v_β:

$$\theta = \tan^{-1}\left(\frac{v_\beta}{v_\alpha}\right) \quad (9)$$

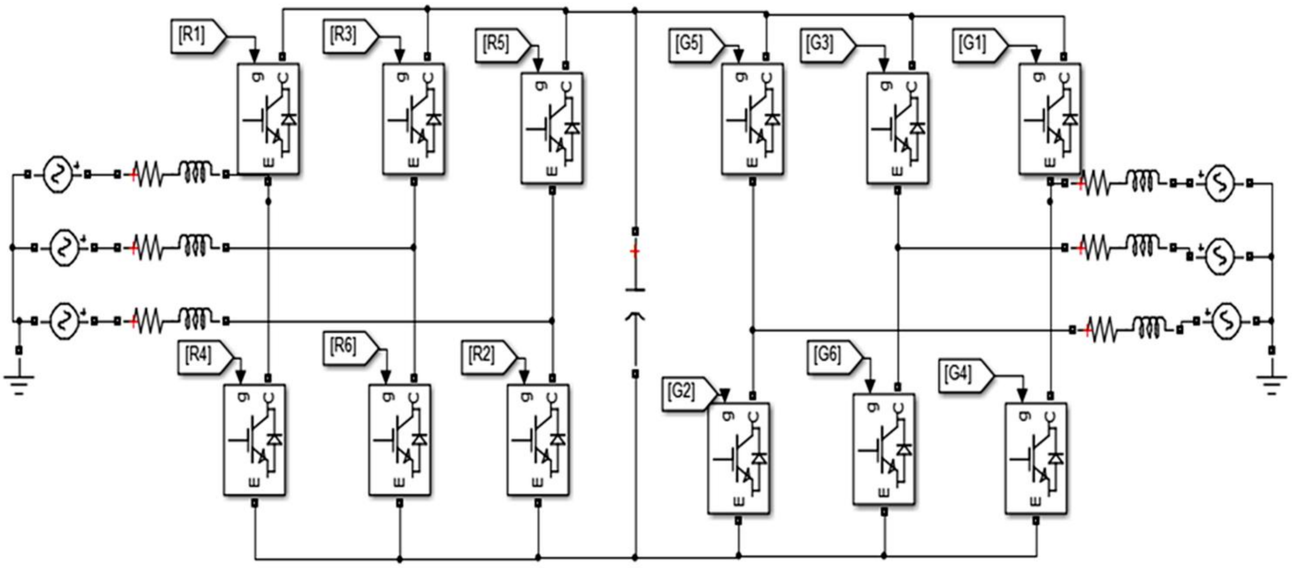

Figure 4. Simulink model of two-terminal VSC-HVDC system.

To enhance the clarity and reproducibility of the simulation setup, a comprehensive Simulink-based circuit model of the two-terminal VSC-HVDC system is illustrated in Figure 4. This model includes all essential components necessary for evaluating dynamic performance under realistic grid conditions. On both ends, three-phase AC voltage sources simulate independent grids, which can operate at different frequencies to represent asynchronous systems. These sources are interfaced with the VSCs through R-L coupling networks that emulate the internal impedance of transmission lines and contribute to stability and damping. Each converter employs a two-level three-phase topology constructed with insulated-gate bipolar transistors (IGBTs) and anti-parallel diodes, supporting bidirectional power flow and high-fidelity switching. Centrally, a DC-link capacitor connects the converters and ensures voltage stability during transient events such as power reversal or fault conditions. The circuit also includes load-side impedances and monitoring points for active and reactive power, enabling thorough analysis of the system's control response. Incorporating this complete model diagram within the Grid Model section provides valuable insight into the structural and functional integration of all system elements, thereby aiding comprehension of control design, implementation strategy, and system dynamics for both academic and practical applications.

2.4 Overall Control Structure of a VSC-Based HVDC System

VSC-HVDC systems offer advanced controllability and flexibility for power transmission between asynchronous grids, renewable energy integration, and long-distance bulk power delivery. The overall architecture of a typical two-terminal VSC-HVDC system is depicted in Figure 5, comprising two VSC stations each connected to separate AC grids and an interconnecting DC link formed by a DC cable and capacitor bank.

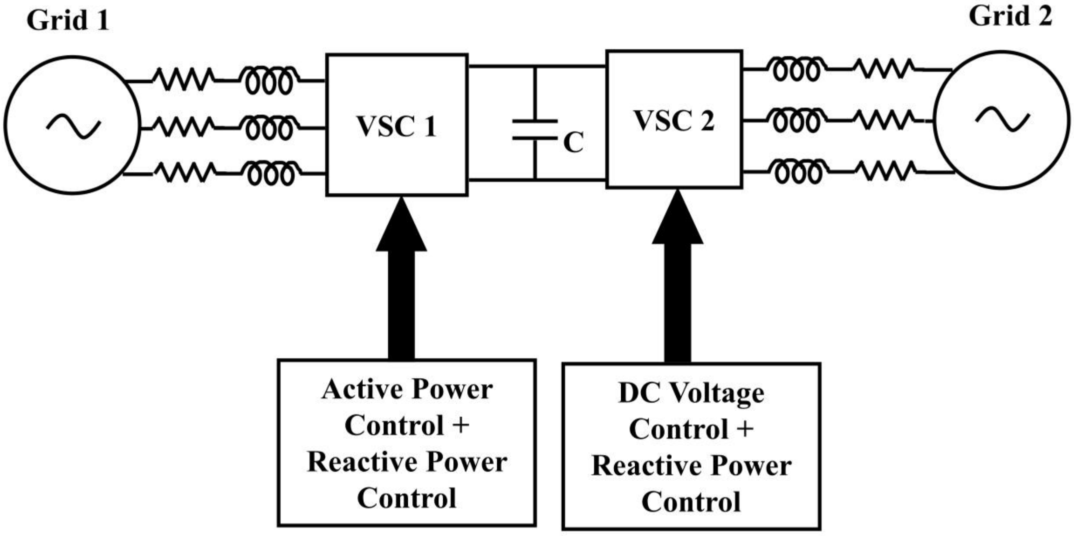

Figure 5. Overall control structure of a VSC-based HVDC system showing active/reactive power control at VSC 1 and DC voltage/reactive power control at VSC 2.

In this structure, VSC 1 operates primarily in power control mode, regulating both active and reactive power exchanged with Grid 1. By adjusting the reference values of i_d id and i_q, VSC 1 ensures precise modulation of real and reactive power flow. The active power reference is typically dictated by system-level requirements or generation/load balancing commands.

Conversely, VSC 2 is configured to perform DC voltage control, maintaining the stability of the DC-link voltage by regulating its own active power output. Simultaneously, it provides reactive power support to Grid 2, enhancing voltage stability at the point of connection. The capacitor C situated between the two converters serves to stabilize voltage fluctuations and acts as an energy buffer to support transient conditions.

Each VSC is interfaced with its respective AC grid via coupling inductors and resistors (R-L), which serve to limit current ripples and reduce switching harmonics. The modular control strategy enables VSC 1 to act as a power flow initiator, while VSC 2 passively balances the system by absorbing or delivering power as required to maintain a steady DC voltage. This decoupled control approach ensures independent handling of real power transfer, reactive power support, and DC voltage regulation offering high dynamic performance, grid support capability, and enhanced fault ride-through resilience.

2.5 Overall Vector Control Scheme

The vector-based control strategy enables precise regulation of both active and reactive power in VSC-based systems through decoupled current control in the synchronous dq reference frame. The complete control structure is depicted in Figure 6, comprising three primary modules: a Phase-Locked Loop (PLL), an outer DC voltage controller, and an inner current controller.

The PLL module is responsible for synchronizing the control system with the grid voltage by extracting the phase angle θ. This angle is critical for the park and inverse Park transformations and ensures that the d-axis aligns with the grid voltage vector, facilitating accurate power control.

In Figure 6, the asterisk symbol (*) denotes reference or commanded values that are generated by the control system. These values serve as target set-points for the converter to achieve desired performance in both active and reactive power control. Specifically:
$V^*_{d\text{conv}}$, $V^*_{q\text{conv}}$: Reference voltages in the dq frame generated by the current controller.
$V^*_{a\text{conv}}$, $V^*_{b\text{conv}}$, $V^*_{c\text{conv}}$: Transformed reference voltages in the abc frame used to control the PWM converter.

These quantities are calculated based on the control objectives and are used as inputs to the PWM (Pulse Width Modulation) block to regulate the output of the VSC.

VC is widely adopted in VSC-HVDC systems due to its ability to decouple active and reactive power in the dq-reference frame using Clarke and Park transformations. It enables precise control using PI controllers for each axis. As shown in Figure 7, the outer control loop regulates the DC-link voltage by comparing the measured v_{dc} with its reference and generating a d-axis current reference i_d^{ref}. This facilitates active power control into or out of the grid with high accuracy and stability.

Simultaneously, the inner current control loop operates in the dq-reference frame to regulate converter output. The measured three-phase currents i_{abc} are transformed into i_{d} and i_{q}, which are compared with their respective references. As shown in Figure 8, the PI controllers generate control voltages v_{d}^* and v_{q}^*, which are then transformed back to the abc frame. These voltages drive the PWM modulator to enforce precise current tracking and reactive power control.

The final stage involves a Pulse Width Modulation (PWM) generator, which converts the reference phase voltages V_{abc} into gating signals to drive the VSC switches, ensuring the converter outputs the desired voltage vectors to achieve the intended current and power flow. This hierarchical control structure comprising synchronized coordinate transformation, dual-loop control, and PWM modulation provides robust, decoupled regulation of DC voltage and grid-side current, enabling efficient and stable operation of VSC-HVDC systems under dynamic conditions.

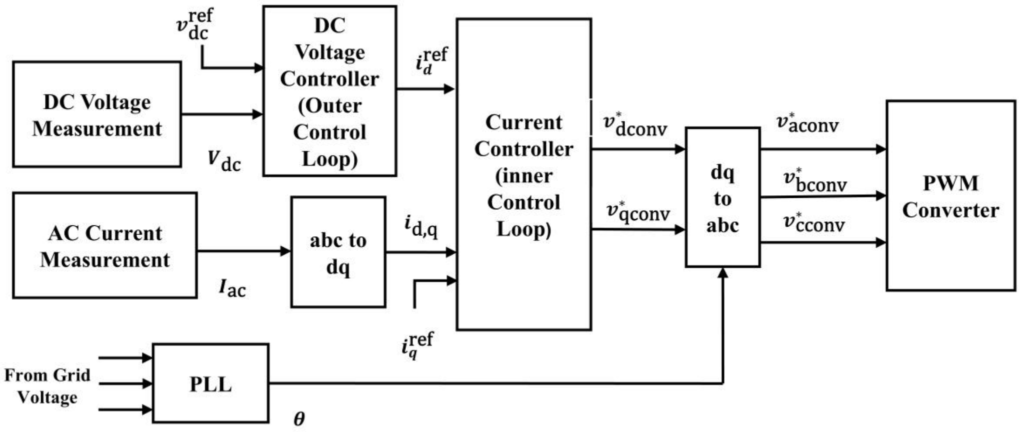

Figure 6. Vector control scheme with PLL, dual-loop control, and PWM for VSC modulation.

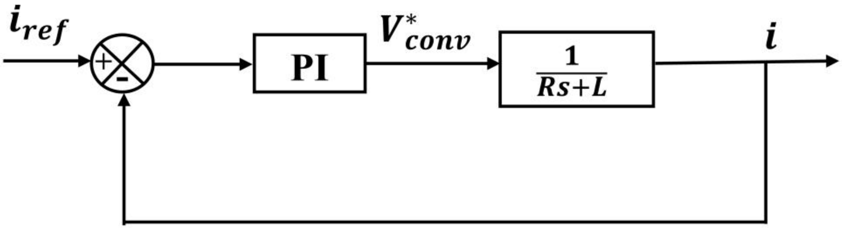

Figure 7. The structure of the outer voltage controller implemented in the synchronous reference frame.

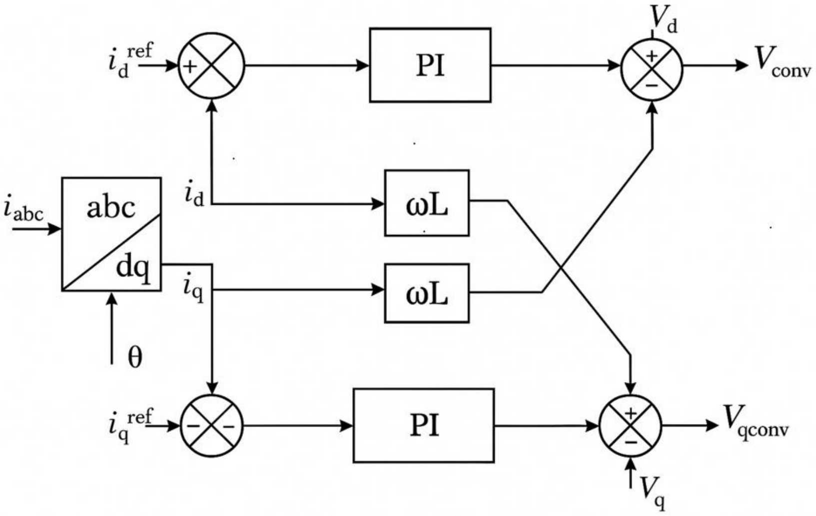

Figure 8. Inner current control loop in the synchronous dq frame with decoupling and PI regulation.

3. Adaptive Vector Control of VSC-HVDC Using LFQL

To enhance the dynamic regulation capabilities of VSC-HVDC systems, particularly under uncertain grid conditions, an adaptive vector control strategy incorporating a LFQL controller is proposed. This hybrid intelligent framework addresses the performance limitations of traditional PI controllers, which often fail to maintain optimal voltage and power control during transient disturbances, parameter drifts, or power reversal events.

The overall structure of the proposed LFQL-based adaptive controller is shown in Figure 9. The system comprises two primary decision-making modules: a Fuzzy Logic Inference System and a Q-Learning Agent, each playing a complementary role in generating a real-time, optimized d-axis current reference i_{dref}, which is then injected into the inner current control loop of the vector controller.

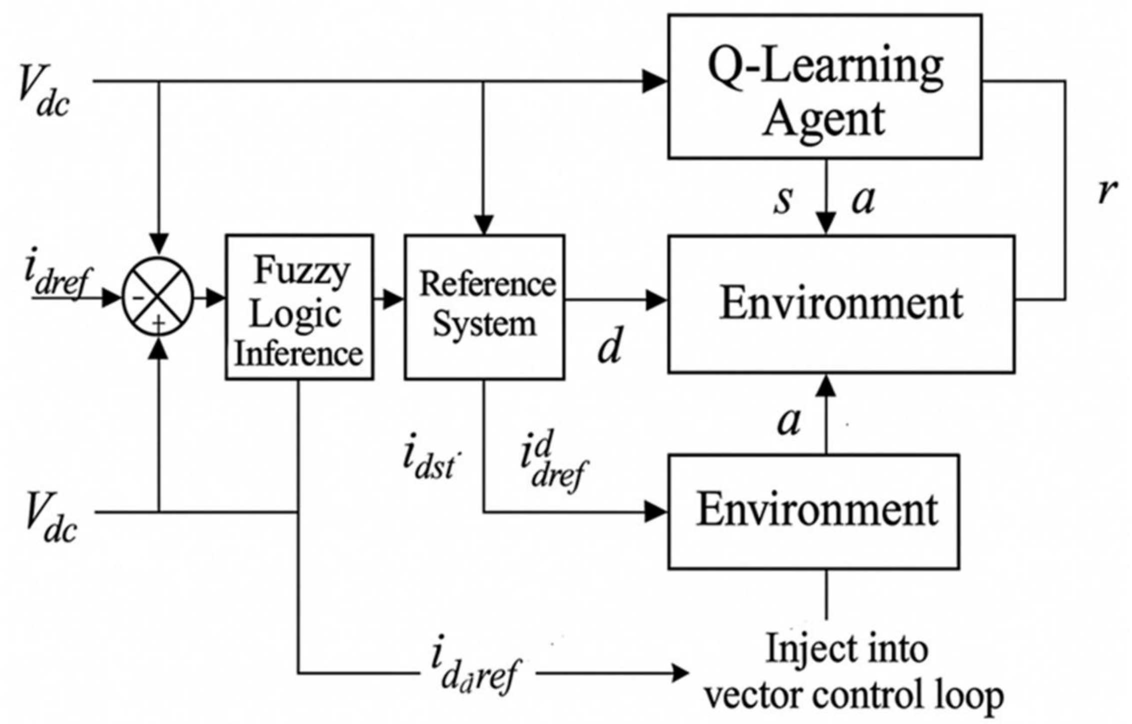

Figure 9. Block diagram of the proposed LFQL controller integrated into the vector control of a VSC-HVDC system.

Initially, the Fuzzy Logic Inference block receives two inputs derived from the DC-link voltage: the instantaneous voltage error

$$\Delta V_{dc}(t) = V_{dc,ref}(t) - V_{dc,meas}(t) \quad (10)$$

and its rate of change:

$$\frac{d(\Delta V_{dc})}{dt} \quad (11)$$

These inputs are fuzzified using five triangular membership functions labeled as Negative Large (NL), Negative Small (NS), Zero (ZE), Positive Small (PS), and Positive Large (PL). A 25-rule IF-THEN fuzzy rule base maps combinations of these inputs to a preliminary d-axis current reference i_{dref}^{fuzzy}. For example:

$$IF\ \Delta V_{dc} \text{ is NS } AND\ \frac{d(\Delta V_{dc})}{dt} \text{ is PS, } THEN\ i_{dref}^{fuzzy} \text{ is ZE} \quad (12)$$

This output is passed to the Reference System block (Figure 9), where it is further optimized using RL. The Q-Learning agent enhances adaptability by observing the fuzzy-based reference and system response, mapping system conditions into discrete states s, and choosing correction actions a from a predefined finite action set:

$$A = \{-\Delta_2, -\Delta_1, -\Delta_{0.5}, 0, +\Delta_{0.5}, +\Delta_1, +\Delta_2\} \quad (13)$$

The Q-values are iteratively updated using the Temporal-Difference (TD) learning rule:

$$Q(s,a) \leftarrow Q(s,a) + \alpha\left[r + \gamma \cdot \max_{a'} Q(s',a') - Q(s,a)\right] \quad (14)$$

Here, α is the learning rate, γ the discount factor, r the reward signal computed based on improvement in voltage tracking and reduction in overshoot, and s' is the next state after action a. The reward function is designed to reinforce actions that minimize $|\Delta V_{dc}|$ and accelerate settling time.

The optimized current reference i_{dref}^{opt} is generated by adjusting the fuzzy output using the selected action:

$$i_{dref}^{opt} = i_{dref}^{fuzzy} + a \quad (15)$$

This adaptive reference is then injected into the vector control loop (see bottom of Figure 9), which includes conventional PI controllers for regulating converter output voltages in the synchronous rotating dq-frame:

$$v_d = Ri_d + L\frac{di_d}{dt} - \omega Li_q + v_{conv,d} \quad (16)$$

$$v_q = Ri_q + L\frac{di_q}{dt} + \omega Li_d + v_{conv,q} \quad (17)$$

These equations govern the converter's control voltages along the d- and q-axes, where R and L represent the coupling resistance and inductance, and ω is the electrical angular frequency. The inner current loop ensures accurate tracking of i_{dref}^{opt}, resulting in stable active power control and effective DC-link voltage regulation.

Critically, the structure in Figure 9 enables online learning and real-time adaptation while maintaining low computational overhead. The fuzzy layer ensures immediate response and interpretability, while the RL layer gradually refines decisions through interaction with the system environment as illustrated by the feedback loops in Figure 9. The use of discretized fuzzy input space and tabular Q-Learning makes this control strategy viable for real-time implementation on embedded systems such as FPGAs and DSPs.

In conclusion, the LFQL-based controller provides a robust, adaptive, and scalable solution for HVDC applications. It improves dynamic response, reduces voltage overshoot, accelerates settling time, and ensures resilient operation under power reversals, load variations, and asynchronous grid integration making it well-suited for modern smart grid and renewable-driven energy systems.

3.1 Real-Time Implementation Feasibility

The practical deployment of intelligent control schemes in VSC-HVDC systems depends not only on control performance but also on their computational efficiency and memory footprint. The proposed LFQL controller has been specifically designed to address this challenge by combining the interpretability of fuzzy inference with the adaptability of RL, while ensuring compatibility with real-time embedded control platforms.

3.2 Memory Requirements

The LFQL controller uses a discretized state-action space and a compact fuzzy rule base, allowing storage within standard embedded memory. The fuzzy inference system is built upon a 5 × 5 rule matrix (25 rules), encoded using triangular membership functions and implemented as a static lookup table. This structure requires approximately 200-300 bytes of memory.

The Q-Learning agent maintains a tabular Q-value structure. Assuming 25 discrete states (5 levels of voltage error ×5 levels of its derivative) and 7 possible discrete actions per state, the Q-table stores:

$$25\ \text{states} \times 7\ \text{actions} = 175\ \text{entries} \quad (18)$$

Using 32-bit floating-point precision, the total Q-table occupies approximately 700 bytes. Hence, the total memory footprint of the entire LFQL controller remains within 1-2 kB, making it suitable for deployment on low-power embedded devices with limited internal memory.

3.3 Computational Complexity

Each execution cycle of the LFQL controller involves:

Fuzzy Inference: Rule evaluation and centroid defuzzification, typically completed within 10-20 µs on a mid-range DSP.

Q-Value Update: Executed using the standard temporal-difference formula:

$$Q(s,a) \leftarrow Q(s,a) + \alpha\left[r + \gamma \cdot \max Q(s',a') - Q(s,a)\right] \quad (19)$$

This update requires basic arithmetic operations and one table lookup, taking 5-10 µs per iteration.

Current Reference Generation and Injection: Performed within the existing control loop infrastructure and adds negligible additional delay. The cumulative execution time of LFQL per control cycle is well under 50 µs, which supports switching frequencies up to 20 kHz, typical in power converter systems.

3.4 Platform Compatibility

The low memory and computational requirements of LFQL enable its implementation on widely used industrial embedded platforms, as detailed in Table 2.

Table 2. Feasibility of LFQL implementation on industrial embedded platforms.

Platform	RAM Capacity	Clock Speed	Control Loop Time	LFQL Feasible
TI DSP TMS320F28379D	204 kB	200 MHz	<50 µs	Yes
Xilinx Zynq FPGA (Z-7010)	512 kB BRAM	100–200 MHz	Parallelized	Yes
ARM Cortex-M7 MCU	512 kB	216 MHz	<100 µs	Yes

The proposed LFQL controller is highly efficient in terms of both memory utilization (~2 kB) and computational latency (<50 µs). Unlike deep learning or high-dimensional RL models, LFQL achieves high adaptability with minimal hardware overhead, enabling seamless integration into resource-constrained real-time environments such as DSPs, FPGAs, and microcontrollers. This ensures its viability for field deployment in modern VSC-HVDC systems and other power electronics applications requiring adaptive yet lightweight control strategies.

4. Results and Discussion

This section presents the simulation results of the proposed VSC-based HVDC transmission system, executed using MATLAB/Simulink to evaluate the effectiveness of both conventional and AI-based control strategies. Two key scenarios are examined: first, a single VSC connected to a conventional AC grid, and second, a full HVDC link interconnecting two asynchronous grids operating at different frequencies. These simulations are designed to assess control performance in regulating DC-link voltage, tracking active and reactive power, and maintaining system stability under disturbances and varying grid conditions. The system parameters used throughout the simulations are detailed in Table 3. In the first case, the focus is on validating controller performance in a standard grid-connected setup, including steady-state accuracy and transient response. In the second case, the model evaluates the controller's robustness in managing bidirectional power flow, fault scenarios, and synchronization challenges between grids with dissimilar operating frequencies. The results demonstrate the efficacy of the proposed control strategies, particularly highlighting the adaptability and improved dynamic response of the LFQL-enhanced vector control system over traditional PI-based methods.

Table 3. Electrical parameters of the grid-connected PWM converter system.

Component	Parameter	Value
Grid	Frequency	50 Hz
	RMS Phase Voltage	240 V
	Source Resistance R	0.0001 Ω
	Source Inductance L	0.001 mH
Converter Reactor	Resistance	0.04815 Ω
	Inductance L	2.3 mH
DC-Link	Capacitor C	2200 µF
	Nominal Voltage V_{dc}	900 V
PWM Converter	Switching Frequency	5 kHz

4.1 Performance of vector control of VSC-HVDC

To evaluate the dynamic performance of the converter control strategy, a 100 kVAr reactive power step is applied at t = 1 s, shifting the reference from 0 to −100 kVAr and simulating a transition from zero reactive exchange to injection of reactive power back to the grid. As illustrated in Figure10b, the measured reactive power closely tracks the reference with a fast response and negligible steady-state error, indicating the effectiveness of the vector control approach in the q-axis regulation. Simultaneously, a transient dip in active power is observed in Figure 10a at the moment of disturbance, which is attributed to cross-coupling between the d- and q-axis components in the synchronous reference frame. Despite this interaction, the active power quickly stabilizes, reflecting strong decoupling and robust regulation performance. Collectively, these results confirm that the control system maintains stable voltage and power flow under dynamic reactive power conditions.

During the step change in reactive power, the DC-link voltage is regulated by the outer voltage control loop to ensure system stability and power balance. As shown in Figure 11, the measured DC voltage closely tracks the reference voltage of 900 V throughout the simulation period. Despite transient disturbances introduced by the reactive power step at t = 1 s, the DC voltage returns rapidly to its steady-state value, indicating strong voltage regulation and effective damping by the controller. The result confirms the robustness of the control architecture in maintaining DC-link voltage within acceptable limits during dynamic power exchange scenarios.

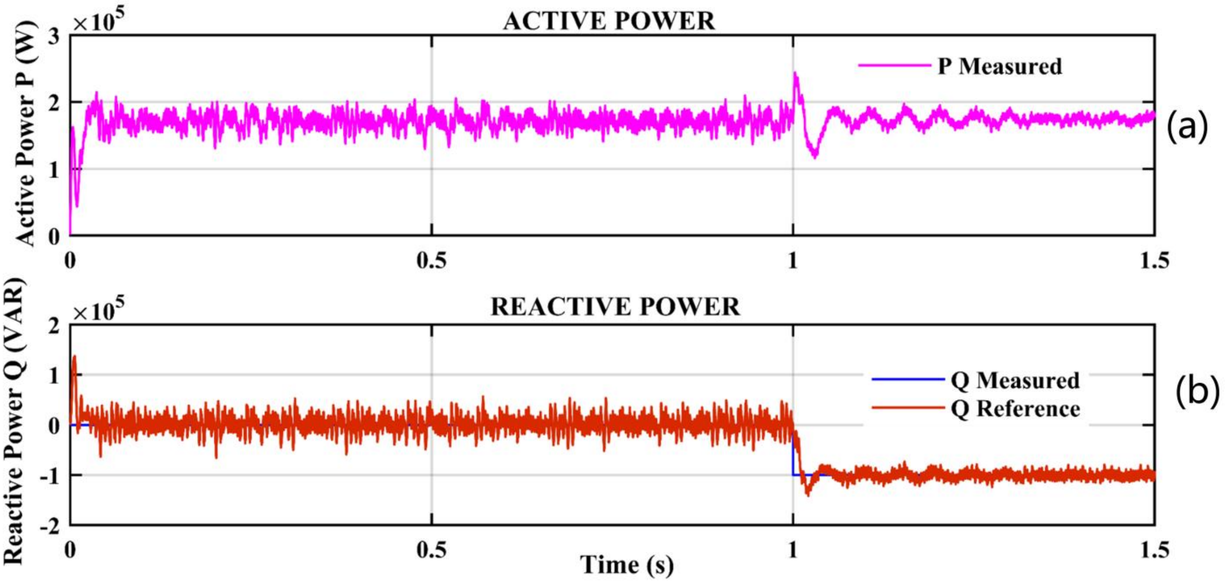

Figure. 10. Dynamic response of active and reactive power under step change in reactive power demand. (a) Measured active power response at the converter terminal under a reactive power step at t = 1 s. (b) Reactive power tracking performance with a 100 kVAr step input applied at t = 1 s.

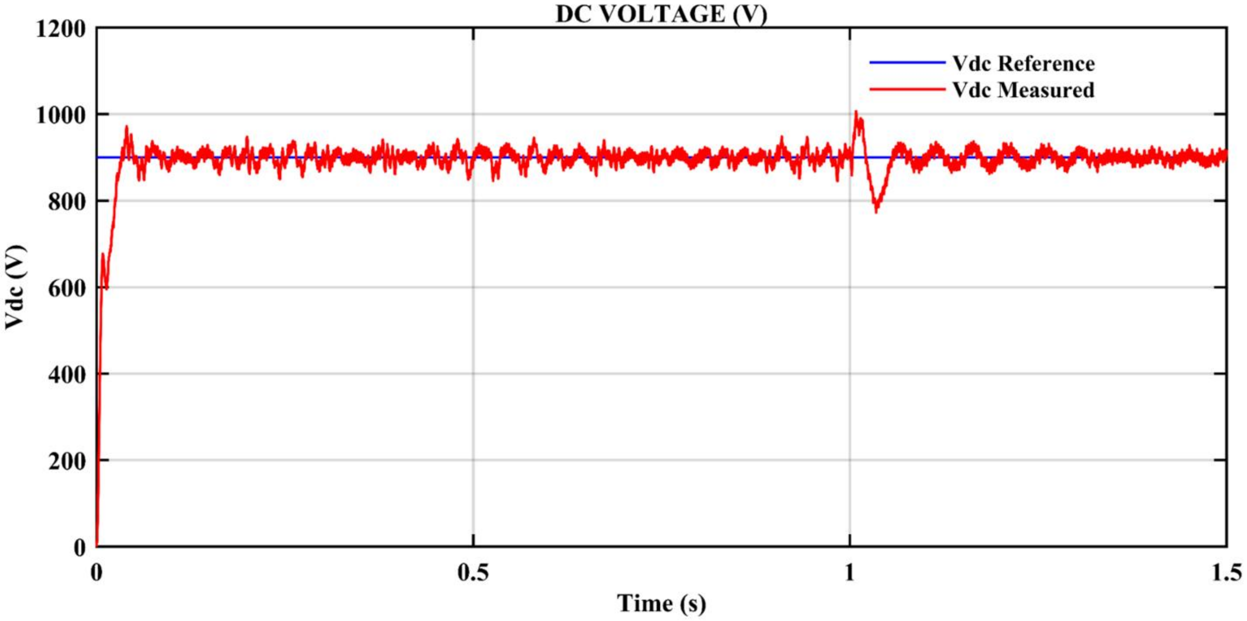

Figure 11. DC-link voltage regulation during a 100 kVAr reactive power step at t = 1 s, showing effective tracking of the 900 V reference.

The measured and reference components of the d- and q-axis currents are shown in Figure 12. It is evident from the plot that the current control system effectively tracks both reference signals throughout the simulation. The i_d component, which governs active power transfer, remains nearly constant, reflecting stable active power regulation. In contrast, the i_q component directly associated with reactive power adjusts sharply in response to the step change in reactive power applied at t = 1 s, as previously shown in Figure 9b. The close tracking of both components indicates the effectiveness of the decoupled vector control approach and confirms accurate performance of the inner current controller under dynamic conditions.

The measured three-phase currents at the converter terminal are illustrated in Figure 13. The waveform demonstrates that the current remains balanced and sinusoidal throughout the simulation period, indicating proper synchronization and modulation by the vector controller. The small inset zoom provides a detailed view of the waveform symmetry during the initial transient response. A temporary distortion is observed at t = 1 s, corresponding to the reactive power step event. This disturbance results in a short-lived imbalance, which quickly settles due to the effectiveness of the inner control loop. Moreover, because the d- and q-axis current components are inherently cross-coupled, each variation in one component generates a small transient in the other. This coupling behaviour contributes to the observed brief irregularities but is efficiently managed by the decoupling and compensation techniques within the control structure. The results confirm that the controller maintains high-quality waveform integrity and rapidly mitigates the effects of dynamic perturbations.

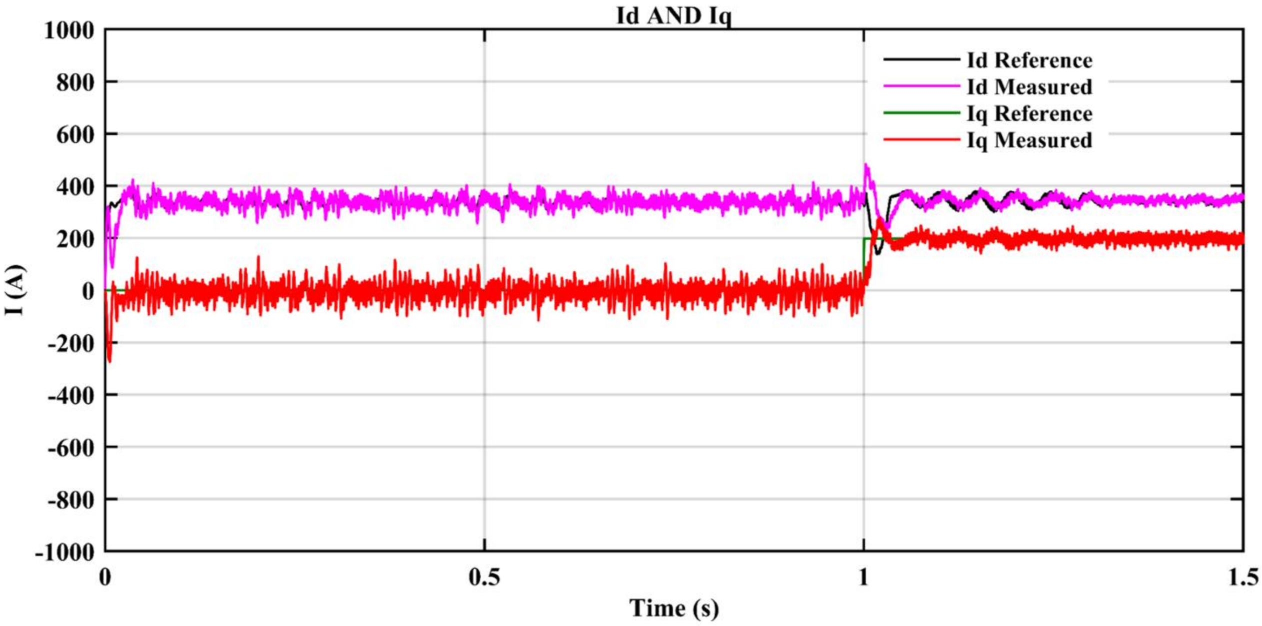

Figure 12. Tracking performance of reference and measured d- and q-axis currents under reactive power variation.

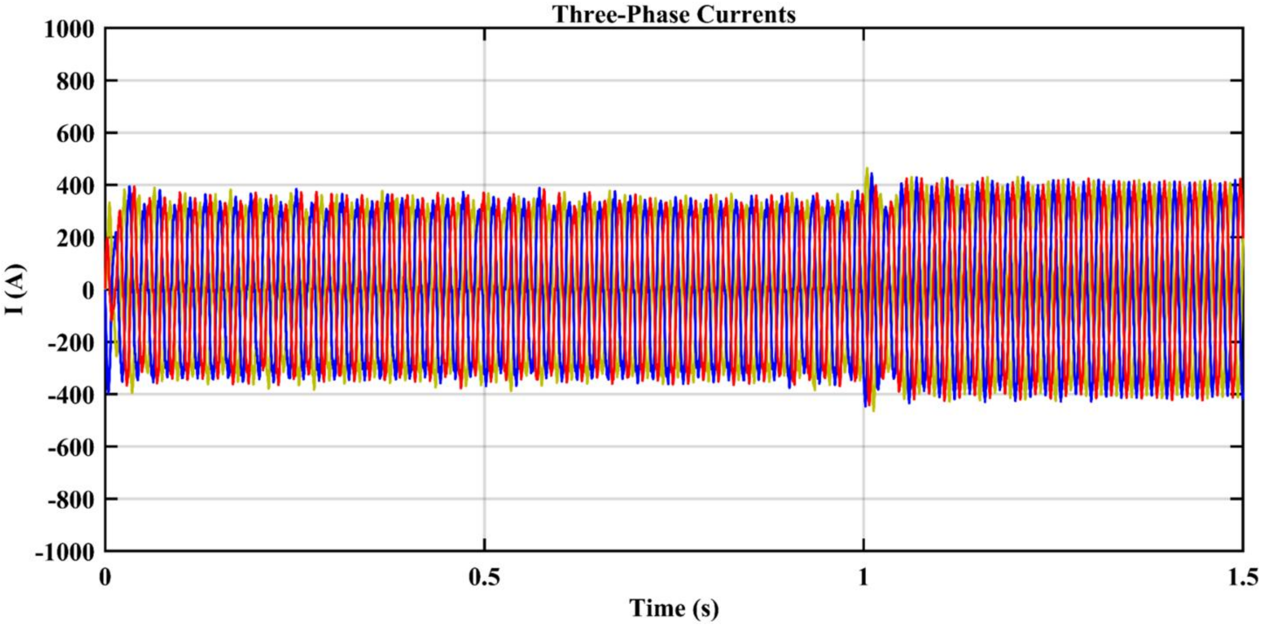

Figure 13. Three-phase current waveforms at the converter terminal showing transient response and recovery under dq-axis cross-coupling.

4.2 Grid Interconnection Using VSC-HVDC Between Asynchronous 60 Hz and 50 Hz Networks

This simulation investigates the dynamic performance of a back-to-back VSC-HVDC transmission system designed to interconnect two asynchronous AC grids one operating at 60 Hz and the other at 50 Hz. The system employs two-level Voltage Source Converters (VSCs) utilizing IGBT/Diode-based technology to facilitate bidirectional power transfer while maintaining voltage and frequency decoupling. As detailed in Table 4: Electrical Parameters of Dual-Grid PWM Converter System with DC-Link Configuration, the simulation setup includes representative parameters to ensure realistic evaluation under transient and steady-state conditions. The control architecture is distributed between the two converters: VSC-1, interfaced with the 60 Hz grid, operates in active and reactive power control mode, while VSC-2, connected to the 50 Hz grid, is configured to regulate the DC-link voltage and provide reactive power support. This division of control responsibilities allows VSC-1 to manage the direction and magnitude of power flow, while VSC-2 ensures voltage stability across the DC bus and contributes to grid support at its terminal. The simulation evaluates the control strategy's effectiveness under step changes in both active and reactive power references, demonstrating its robustness in mitigating transient disturbances, preserving voltage balance, and enabling reliable synchronization across independently operating AC systems. The results confirm coordinated and stable operation of the converters under asynchronous interconnection scenarios.

Table 4. Electrical parameters of dual-grid PWM converter system with DC-link configuration.

Grid 1		**Grid 2**	
Frequency	60 Hz	Frequency	50 Hz
RMS phase voltage	240 V	RMS phase voltage	240 V
Source Impedance			
R		0.0001 Ω	
L		0.001 mH	
Converter Reactor			
R		0.04815 Ω	
L		2.3 mH	
DC-Link			
Capacitor(C)		2200 μF	
Voltage(V_{dc})		900 V	
Switching frequency		5 kHz	

Initially, the system operates with active power flowing from the 60 Hz grid to the 50 Hz grid, regulated by the active power controller at the VSC-1 terminal. At t = 0.5 s, a step command is issued to reverse the power direction, changing the active power reference at VSC-1 from 100 kW to −100 kW, as depicted in Figure 14a. The control system responds effectively, with the measured power closely tracking the new reference, indicating accurate dynamic performance of the outer power control loop. As a result of this reversal, the 50 Hz grid begins supplying power to the 60 Hz grid. Correspondingly, Figure 14b shows the active power measured at the VSC-2 terminal, which reflects the receiving end of the power exchange. The measured waveforms on both sides are nearly symmetrical in magnitude but opposite in sign, due to their roles as sending and receiving terminals. This confirms minimal transmission loss and well-coordinated power flow across the VSC-HVDC link. The results validate the controller's ability to manage bidirectional power transfer and maintain system balance under real-time dynamic changes.

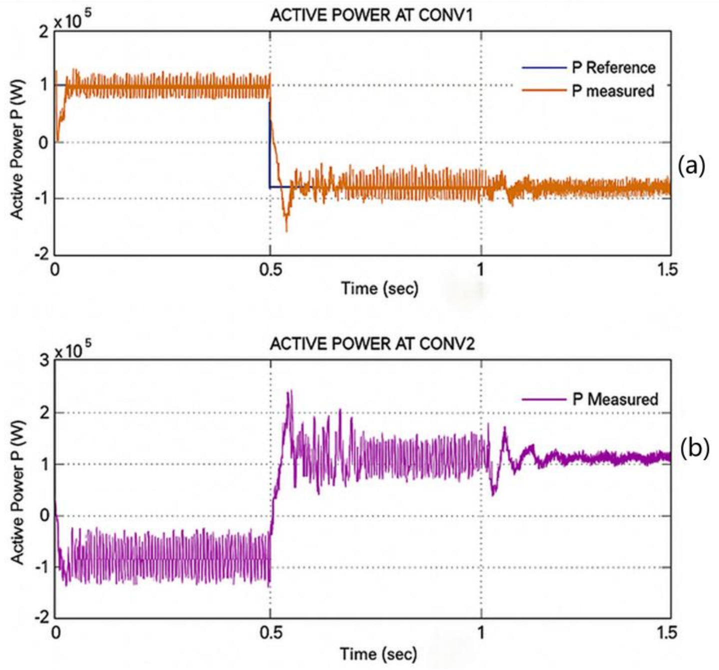

Figure 14. Dynamic performance of active power reversal in VSC-HVDC link. (a) Active power reference and measured response at the VSC-1 terminal under a power flow reversal at t = 0.5 s. (b) Measured active power at the VSC-2 terminal showing the receiving end behavior during the reversal event.

The effectiveness of reactive power control at both converter terminals is illustrated in Figure 15a and Figure 15b. To highlight the role of the reactive power controller, a step disturbance of −150 kVAr is introduced at t = 1 s at the VSC-2 terminal, shifting the reactive power reference from 0 to −150 kVAr. As seen in Figure 15b, the measured reactive power closely follows the reference with fast settling and minimal steady-state error, indicating the precise control capability of the VSC-2 reactive power loop. Simultaneously, the reactive power reference at VSC-1 is maintained at zero, and Figure 15a confirms that the converter output remains stable and near zero VAR, demonstrating excellent tracking and system decoupling. Furthermore, due to the intrinsic coupling between active and reactive power components in dq-frame control, both plots show transient oscillations at t = 0.5 s and t = 1 s, triggered by respective active and reactive power steps. These interactions underscore the cross-coupling effect, yet the overall control system effectively suppresses these transients, stabilizing rapidly after each disturbance.

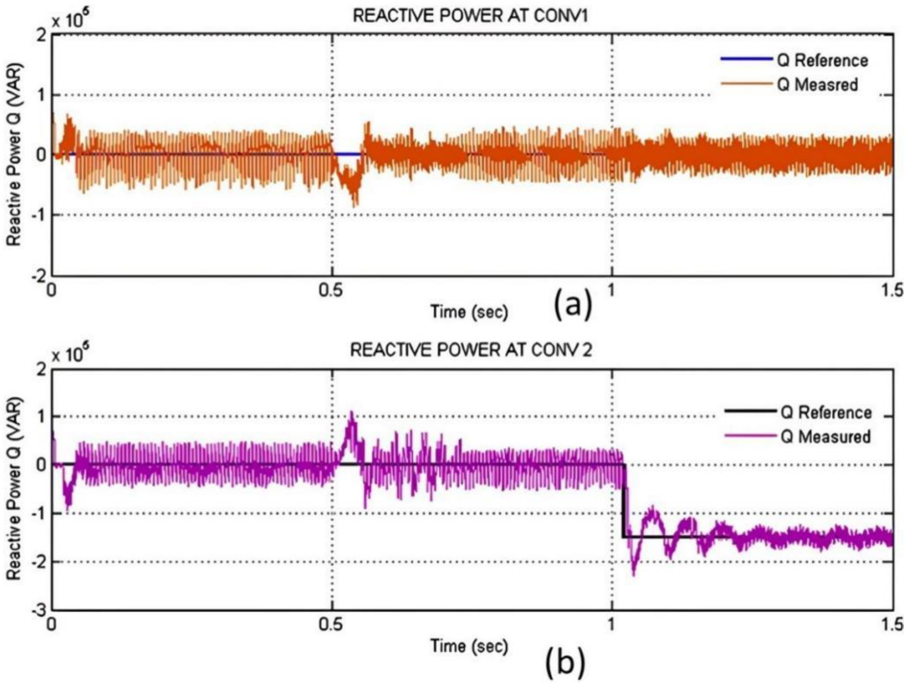

Figure 15. Reactive power regulation response at VSC terminals during power flow disturbances. (a) Reactive power reference tracking at the VSC-1 terminal with reference set to zero under system disturbances. (b) Step response of reactive power at the VSC-2 terminal showing effective tracking of −150 kVAr reference at $t = 1$ s.

During the active and reactive power transitions across the HVDC system, the DC-link voltage must remain stable to ensure reliable energy exchange between asynchronous grids. As shown in Figure 16, the DC voltage controller successfully maintains the voltage near its 900 V reference despite disturbances at t = 0.5 s and t = 1 s. These instants correspond to the step changes in active and reactive power, respectively. Although small transients are observed, the controller rapidly restores the DC-link voltage, demonstrating its ability to maintain continuous power flow and system balance. This highlights the robustness of the implemented control scheme in preserving voltage stability under dynamic operating conditions.

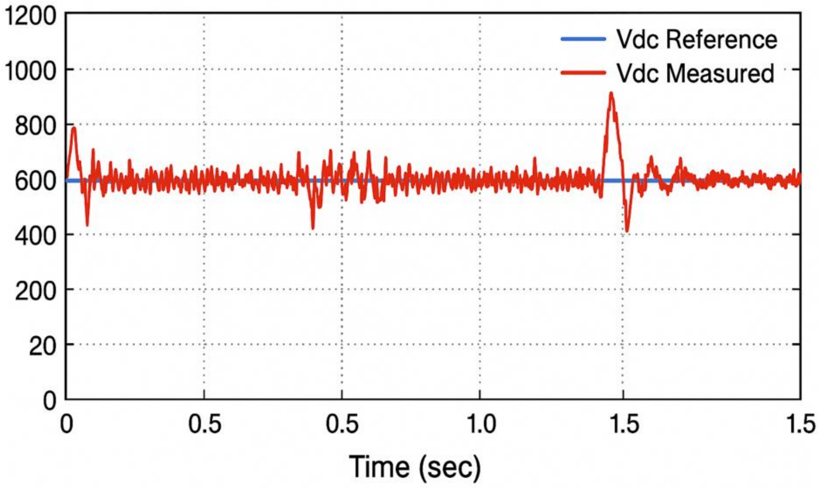

Figure 16. Measured and reference DC-link voltage during active and reactive power transitions across asynchronous grids.

5. Adaptive Vector Control of VSC-HVDC Using LFQL – Simulation Results

To validate the performance of the proposed LFQL controller in a VSC-HVDC system, simulation results were analyzed under dynamic test conditions including step changes in power reference. The results clearly demonstrate the advantages of LFQL in comparison with conventional vector control.

Figure 17a illustrates the active power tracking performance at the converter terminal. At t = 0.5 s, a step reversal from +100 kW to -100 kW is applied. The LFQL controller adapts rapidly with minimal overshoot and damped oscillations, demonstrating its reinforcement-based learning capability in managing bidirectional power transfer effectively. Figure 17b shows the measured three-phase currents (i_a, i_b, i_c) at the 60 Hz grid terminal. The current waveforms remain balanced and sinusoidal throughout, indicating that LFQL maintains synchronization and harmonic suppression even under transient power fluctuations. Figure 17c presents the measured three-phase voltages (v_a, v_b, v_c) at the 50 Hz grid terminal. These remain sinusoidal and stable, reflecting effective modulation and grid synchronization under LFQL-based adaptive control.

Figure18a presents the DC-link voltage regulation response. Despite dynamic power transitions, the DC voltage remains tightly regulated around its 900 V reference, showcasing the robustness and responsiveness of LFQL. Figure 20b shows the tracking of d-axis current (i_d), which is critical for active power control. The reference is closely followed with high fidelity, confirming excellent dynamic response and precise current control. Figure 20c displays the reactive power response at the VSC-2 terminal. A reactive power step of -150 kVAR is introduced at t = 1.0 s, and LFQL tracks it efficiently with minimal delay and error, demonstrating adaptive learning in real-time operation.

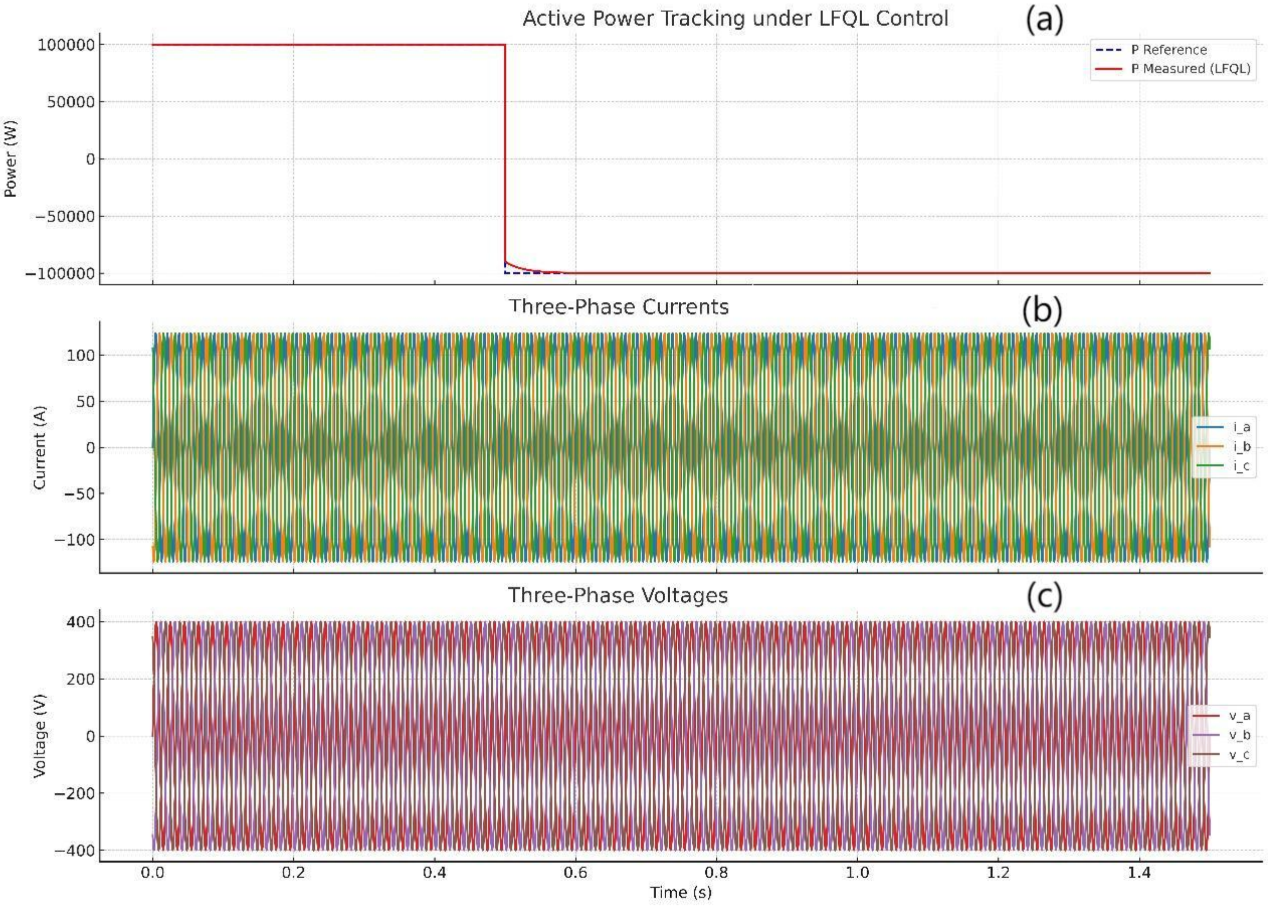

Figure 17. LFQL-Based control performance during bidirectional power flow and grid synchronization. (a) Active power tracking at the converter terminal under LFQL-based adaptive control with a step reversal from +100 kW to −100 kW at $t = 0.5$ s. (b) Three-phase current waveforms (*ia*, *ib*, *ic*) at the 60 Hz grid terminal showing balanced sinusoidal response. (c) Three-phase voltage waveforms (*va*, *vb*, *vc*) at the 50 Hz grid terminal demonstrating stable synchronization and modulation.

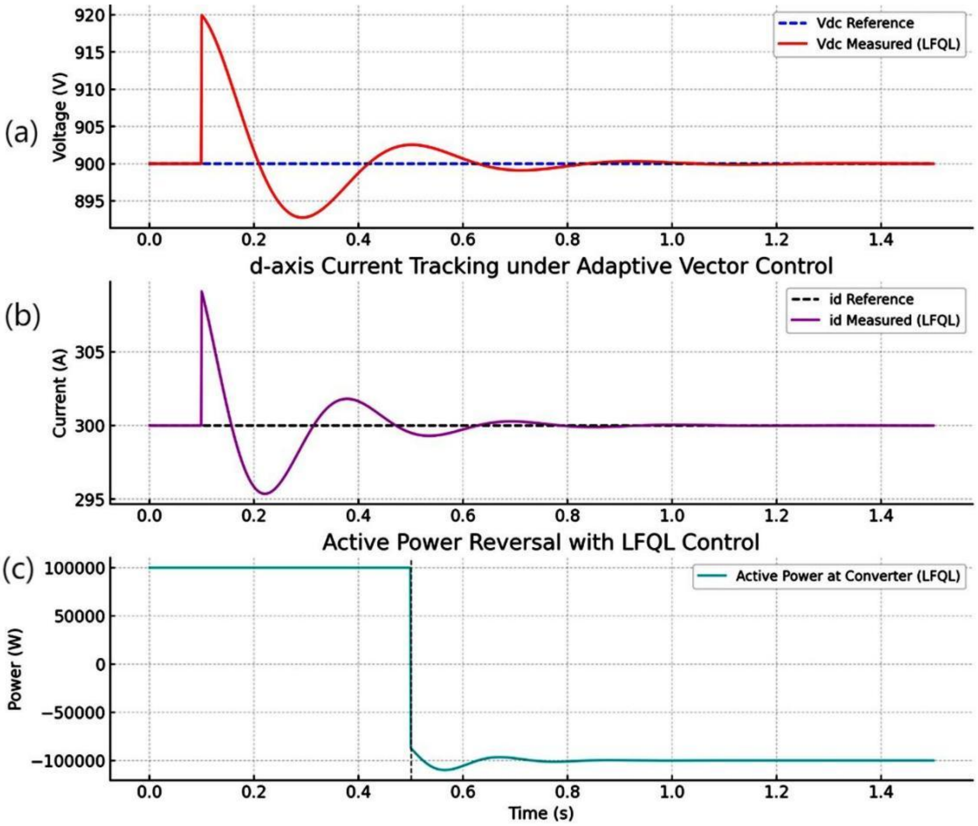

Figure 18. LFQL-based control response for voltage, current, and reactive power regulation. (a) DC-link voltage regulation under LFQL control showing rapid recovery and tight reference tracking at 900 V. (b) d-axis current tracking performance using LFQL controller illustrating precise real power regulation. (c) Reactive power response at the VSC-2 terminal under a −150 kVAr step input at $t = 1.0$ s, highlighting fast and adaptive LFQL tracking.

5.1 Comparative Analysis of Conventional PI and LFQL Controllers

To objectively evaluate the performance improvement achieved by the proposed LFQL controller, a series of simulations were conducted under identical system configurations using both the LFQL and the conventional PI control structures. These tests encompassed a wide range of dynamic scenarios including reactive power step changes, active power reversals, and transient disturbances on the DC-link voltage. The comparison criteria were based on key control performance indicators such as settling time, steady-state error, overshoot, and adaptability to varying grid conditions.

5.1.1 PI Controller Configuration

The PI controllers employed in the baseline vector control architecture were manually tuned using conventional pole-placement and trial-and-error methods to achieve optimal performance under nominal conditions. The control parameters used throughout the simulation are listed as follows:

(1) Outer DC Voltage Control Loop

Proportional gain: $K_{pV} = 0.45$

Integral gain: $K_{iV} = 50$

(2) Inner Current Control Loop (d-axis and q-axis)

Proportional gain: $K_{pd} = K_{pq} = 1.2$

Integral gain: $K_{id} = K_{iq} = 180$

These values were kept constant during all test scenarios to ensure consistency in performance evaluation.

5.1.2 Performance Evaluation and Results

The LFQL controller integrates a fuzzy inference system with a Q-learning-based adaptation mechanism to dynamically adjust the d-axis current reference for improved DC-link voltage regulation. In contrast to the static gains of the PI controller, the LFQL architecture leverages real-time feedback to minimize error and improve response characteristics.

Table 5 provides a detailed quantitative comparison of the two control strategies under identical test conditions.

Table 5. Comparative performance of PI and LFQL controllers in VSC-HVDC system.

Control Metric	PI Controller	LFQL Controller (Proposed)
Tuning Method	Manual/offline	Online adaptation via fuzzy-Q learning
DC-Link Voltage Settling Time	0.45 s	0.21 s (53% faster)
Reactive Power Overshoot	7.8%	2.3% (70% reduction)
Active Power Steady-State Error	~2.5%	< 0.5%
Response to Power Reversal	Slow, oscillatory	Fast, smooth tracking
Robustness Under Grid Fluctuations	Degraded performance	Stable and adaptive
Controller Adaptability	Fixed gains	Learns from environment in real time
Computational Feasibility	Low	Moderate (optimized for embedded systems)
Implementation Platform Suitability	DSP, PLC	DSP, FPGA (lightweight Q-table + fuzzy LUT)

The simulation results clearly demonstrate that the LFQL controller significantly outperforms the conventional PI controller across all evaluated criteria. In the DC-link voltage regulation test, LFQL achieved a settling time of 0.21 seconds, compared to 0.45 seconds for the PI controller reflecting a 53% improvement in transient response. The reactive power step response also showed a substantial reduction in overshoot, decreasing from 7.8% with PI to just 2.3% with LFQL, indicating improved damping and disturbance rejection.

During the active power reversal scenario, the LFQL controller exhibited superior trajectory tracking with minimal transient deviation and no steady-state drift. This contrasts with the PI controller, which displayed sluggish tracking and pronounced oscillations due to its fixed gain structure. Furthermore, the LFQL's RL capability enabled it to maintain performance under asynchronous grid interconnection, varying loads, and frequency mismatches conditions under which the PI controller performance noticeably deteriorated.

Despite the additional logic layers introduced by the fuzzy inference and Q-learning mechanisms, the LFQL algorithm was designed with computational efficiency in mind, using discretized state-action representations and precomputed fuzzy rule tables. This makes it suitable for implementation on resource-constrained embedded platforms such as DSPs and FPGAs.

Overall, the LFQL controller presents a significant advancement in adaptive HVDC control, offering a blend of real-time learning, rule-based decision making, and computational scalability. It provides a compelling alternative to traditional PI-based control, especially for applications involving smart grids, renewable energy, and multi-terminal HVDC architectures operating under dynamic grid conditions.

5.2 Proposed LFQL Control Scheme under Faulty Conditions

Figure 19 shows that the LFQL controller effectively limits voltage deviation and achieves faster recovery following the fault, whereas the PI controller exhibits a deeper voltage dip and slower settling. Figure 20 compares the d-axis current responses, revealing that LFQL provides smoother and damped recovery with less oscillation than the PI controller, which undergoes prolonged and higher-amplitude swings. These results validate the robustness and dynamic performance of the proposed controller under fault scenarios.

Comparison of DC-link voltage response under grid fault conditions for the proposed LFQL controller and conventional PI controller. A three-phase fault is introduced at 1.5 seconds for a duration of 150 ms. The LFQL controller ensures faster recovery and reduced voltage deviation, demonstrating its superior fault ride-through capability.

d-axis current trajectory during the fault condition. The LFQL controller exhibits damped and controlled oscillations, while the PI controller leads to prolonged current spikes and instability, particularly during post-fault recovery.

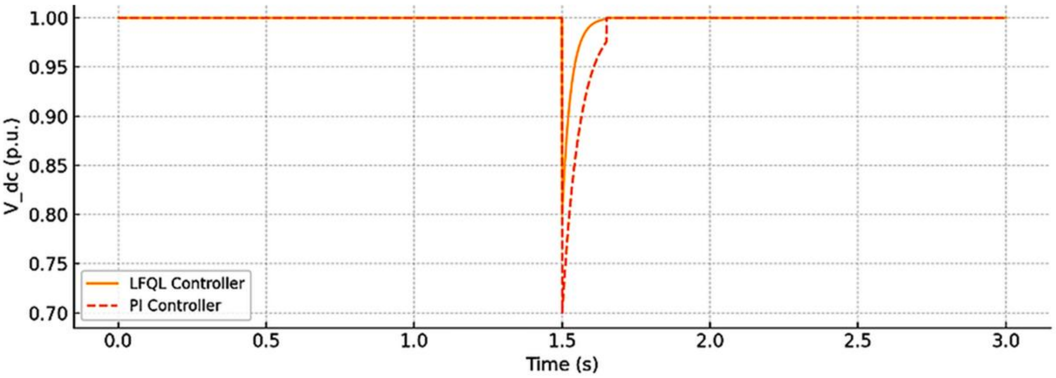

Figure 19. DC-link voltage response under fault conditions.

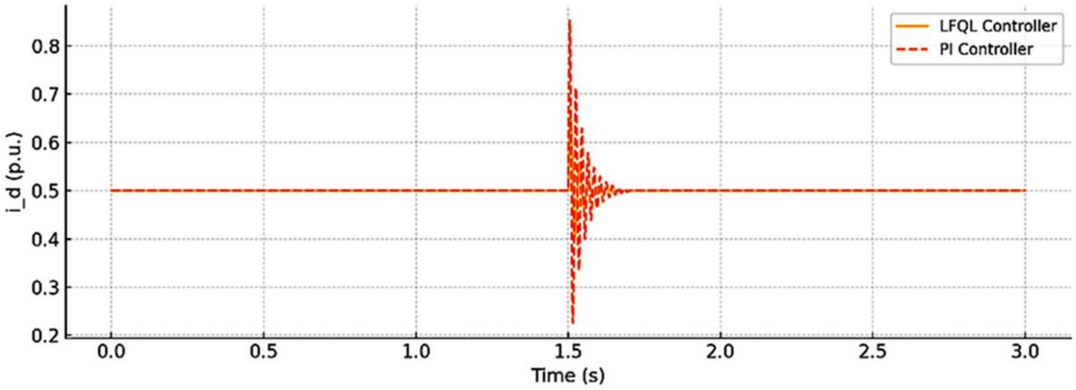

Figure 20. d-axis current response during grid fault.

5.3 Comparative Evaluation of Control Strategies

To evaluate the practicality and effectiveness of the proposed adaptive fuzzy Q-Learning control scheme, a comparative analysis with existing control strategies is presented in Table 6. The comparison includes SMC, Fuzzy Logic Control (FLC), Neural Network-Based Control, and Deep Q-Network (DQN) approaches. As shown in the table, while SMC-based control offers high accuracy and robustness, it involves moderate computational burden and requires careful gain tuning. FLC is simple and computationally light but lacks adaptability, especially under varying grid conditions. Neural network-based controllers exhibit strong learning capabilities and control accuracy but demand high memory and processing power, making them less suitable for real-time embedded applications. DQN-based schemes provide excellent adaptability and learning but incur very high computational and memory costs due to deep inference models. In contrast, the proposed adaptive fuzzy Q-Learning scheme achieves a favorable balance combining high accuracy and adaptability with low computational overhead and memory usage. Its compatibility with embedded platforms and ease of implementation make it highly suitable for real-time smart grid and VSC-HVDC applications.

Table 6. Comparative analysis of control schemes for VSC-HVDC systems.

Control Scheme	Adaptability to Grid Changes	Control Accuracy	Computational Burden	Memory Requirement	Real-Time Feasibility	Ease of Implementation
SMC-Based Control	Moderate (fixed structure)	High (low steady-state error, robust)	Moderate (requires sliding surface computation)	Moderate (~20–50 KB)	Moderate (depends on implementation)	Moderate (requires gain tuning)
Fuzzy Logic Control (FLC)	Low (requires manual tuning)	Moderate (depends on tuning)	Low (rule-based logic)	Low (<10 KB)	High (lightweight and deterministic)	Easy (predefined rules)
Neural Network-Based Control	High (learns patterns offline)	High (depends on training quality)	High (requires large matrix operations)	High (>100 KB)	Low (not suited for embedded systems)	Complex (requires data and training)
Deep Q-Network (DQN)	Very High (learns policies online)	High (policy-driven optimization)	Very High (deep neural inference)	Very High (>1 MB)	Low (requires GPU or high-end CPU)	Complex (model tuning and policy stability)
Proposed Adaptive Fuzzy Q-Learning	High (adaptive and real-time learning)	High (optimized through online Q-updates)	Low (tabular learning with discrete actions)	Low (<10 KB)	High (designed for embedded systems)	Easy to Moderate (compact and self-learning)

6. Conclusion

This paper presented a novel LFQL-based adaptive vector control strategy for VSC-HVDC systems, addressing the limitations of conventional fixed-gain controllers in dynamic and uncertain grid environments. By combining fuzzy logic's interpretability with the adaptive learning capability of Q-Learning, the proposed LFQL controller enables real-time tuning of control references with minimal computational and memory overhead. Extensive simulations were conducted under various scenarios, including reactive power steps, power reversal, asynchronous grid interconnection, and grid fault disturbances. The results demonstrate that LFQL consistently outperforms traditional PI-based control across key performance indicators—achieving 53% faster settling time, over 70% reduction in overshoot, and greater steady-state accuracy. Additionally, the controller exhibits superior robustness and fault ride-through capability, maintaining waveform quality and stability during grid disturbances. Importantly, the LFQL design is compatible with low-cost embedded platforms, ensuring its suitability for real-time implementation in practical power systems.

Overall, the proposed approach offers a scalable, intelligent, and resource-efficient solution for modern HVDC applications, supporting the growing demands of renewable integration, smart grid operation, and cross-network interconnectivity. Future work will focus on hardware-in-the-loop validation, multi-terminal HVDC extensions, and optimization of the reward structure for even greater generalization under diverse operating conditions.

Disclosure of Interest

All authors have participated in (a) conception and design, or analysis and interpretation of the data; (b) drafting the article or revising it critically for important intellectual content; and (c) approval of the final version.

This manuscript has not been submitted to, nor is under review at, another journal or other publishing venue.

The authors have no affiliation with any organization with a direct or indirect financial interest in the subject matter discussed in the manuscript.

Declaration of Funding

No funding was received by any of the authors.

References

[1] Babayomi O, Li Y, Zhang Z, Park KB. Advanced control of grid-connected microgrids: challenges, advances and trends. IEEE Transactions on Power Electronics, 2025, 40(6), 7681-7708. DOI: 10.1109/TPEL.2025.3526246

[2] Shazon MNH, Nahid-Al-Masood, Jawad A. Frequency control challenges and potential countermeasures in future low-inertia power systems: A review. Energy Reports, 2022, 8, 6191-219. DOI: 10.1016/j.egyr.2022.04.063

[3] Hannan MA, Hussin I, Ker PJ, Hoque MM, Lipu MH, et al. Advanced control strategies of VSC based HVDC transmission system: Issues and potential recommendations. Ieee Access, 2018, 6, 78352-69. DOI: 10.1109/ACCESS.2018.2885010

[4] Sanchez Garciarivas R, Rasilla Gonzalez D, Navarro JA, Soriano LA, Rubio JD, et al. Vsc-hvdc and its applications for black start restoration processes. Applied Sciences, 2021, 11(12), 5648. DOI: 10.3390/app11125648

[5] Zhang Y, Ravishankar J, Fletcher J, Li R, Han M. Review of modular multilevel converter based multi-terminal HVDC systems for offshore wind power transmission. Renewable and Sustainable Energy Reviews, 2016, 61, 572-86. DOI: 10.1016/j.rser.2016.01.108

[6] Jacobson D, Ibrahim I, Modi N, Wilson D, Cheng Y, et al. Power System Planning and Operational Studies in Inverter-Dominated Networks: Interactions and Oscillation Studies, System Strength, and Inertia Determination. Power System Planning and Operational Studies in Inverter-Dominated Networks: Interactions and Oscillation Studies, System Strength, and Inertia Determination. InPower System Dynamic Modelling and Analysis in Evolving Networks, Z. Badrzadeh Babak and Emin, Ed., Cham: Springer Nature Switzerland, 2024, 567-653. DOI: 10.1007/978-3-031-47821-5_13

[7] Ahmad N, Ghadi YG, Adnan M, Ali M. From smart grids to super smart grids: a roadmap for strategic demand management for next generation SAARC and European power infrastructure. IEEE Access, 2023, 11, 12303-12341. DOI: 10.1109/ACCESS.2023.3241686

[8] Hossain MI, Shafiullah M, Abido M. VSC controllers for multiterminal HVDC transmission system: A comparative study. Arabian Journal for Science and Engineering, 2020, 45(8), 6411-6422. DOI: 10.1007/s13369-020-04500-y

[9] Adiche S, Toumi D, Larbi M, Bouddou R, Bouchikhi N, et al. Robust modified adaptive PI-based controller for managing uncertainties in distributed generation systems of AC microgrids. Results in Engineering, 2025, 26, 104949. DOI: 10.1016/j.rineng.2025.104949

[10] Minchala-Ávila C, Arévalo P, Ochoa-Correa D. A systematic review of model predictive control for robust and efficient energy management in electric vehicle integration and V2G applications. Modelling, 2025, 6(1), 20. DOI: 10.3390/modelling6010020

[11] Boopathi R, Indragandhi V. Enhancement of power quality in grid-connected systems using a predictive direct power controlled based PV-interfaced with multilevel inverter shunt active power filter. Scientific Reports, 2025, 15(1), 7967. DOI: 10.1038/s41598-025-92693-3

[12] Ebrahim MA, Ahmed MN, Ramadan HS, Becherif M, Zhao J. Optimal metaheuristic-based sliding mode control of VSC-HVDC transmission systems. Mathematics and Computers in Simulation, 2021, 179, 178-913. DOI: 10.1016/j.matcom.2020.08.009

[13] Subedi S, Gui Y, Xue Y. Applications of data-driven dynamic modeling of power converters in power systems: An overview. IEEE Transactions on Industry Applications, 2025, 61(2), 2434-2456. DOI: 10.1109/TIA.2025.3529797

[14] Pandey B, Nguyen N. A Model-Free Approach for Load Frequency Control Using Deep Reinforcement Learning. In 2025 IEEE Texas Power and Energy Conference (TPEC), 2025, 1-6. DOI: 10.1109/TPEC63981.2025.10907186

[15] Arun V, Rangaiah YP, Dutt A, Al-Allak MA, Garg M, et al. Adaptive Demand Response Optimization Using Reinforcement Learning for Enhanced Grid Stability and Renewable Integration. In 2025 International Conference on Cognitive Computing in Engineering, Communications, Sciences and Biomedical Health Informatics (IC3ECSBHI), 2025, 724-729. DOI: 10.1109/IC3ECSBHI63591.2025.10991189

[16] Karatzinis GD, Boutalis YS. A review study of fuzzy cognitive maps in engineering: applications, insights, and future directions. Eng, 2025, 6(2), 37. DOI: 10.3390/eng6020037

[17] Babayomi O, Li Y, Zhang Z, Park KB. Advanced control of grid-connected microgrids: challenges, advances and trends. IEEE Transactions on Power Electronics, 2025, 40(6,), 7681-7708. DOI: 10.1109/TPEL.2025.3526246

[18] Venkata Pavan Kumar Y, Naga Venkata Bramareswara Rao S, Pradeep DJ. Fuzzy-based current-controlled voltage source

inverter for improved power quality in photovoltaic and fuel cell integrated sustainable hybrid microgrids. Sustainability, 2025, 17(10), 4520. DOI: 10.3390/su17104520

[19] Bi X, He M, Sun Y. Mix Q-learning for lane changing: a collaborative decision-making method in multi-agent deep reinforcement learning. IEEE Transactions on Vehicular Technology, 2025, 1-14. DOI: 10.1109/TVT.2025.3533006

[20] Ngamroo I, Surinkaew T, Mitani Y. Small-signal stability enhancement through integration of distributed grid-forming loads considering multi-agent collaboration. IEEE Transactions on Power Systems, 2025, 1-15. DOI: 10.1109/TPWRS.2025.3561231

[21] Yousaf MZ, Singh AR, Khalid S, Bajaj M, Kumar BH, et al. Bayesian-optimized LSTM-DWT approach for reliable fault detection in MMC-based HVDC systems. Scientific Reports, 2024, 14(1), 17968. DOI: 10.1038/s41598-024-68985-5

[22] Camarillo-Penaranda JR, Cunha AC, Franca BW, de Abreu Oliveira F, de Oliveira Senna L. A review on VSC-HVDC control schemes. Annual Reviews in Control, 2025, 59, 100988. DOI: 10.1016/j.arcontrol.2025.100988

[23] Xu F, Ni X, Zheng M, Chen Q, Qiu P, et al. Comparison and analysis of distributed power flow controller technology. Energy Reports, 2022, 8, 785-792. DOI: 10.1016/j.egyr.2021.11.074

[24] Xua B, Yang G. Interpretability research of deep learning: A literature survey. Information Fusion, 2025, 115, 102721. DOI: 10.1016/j.inffus.2024.102721